Effects of temperature and dose rate on ion-irradiated γ-$LiAlO_2$ pellets

Weilin Jiang,[1,a)], Libor Kovarik,[1] Zihua Zhu,[1] Karen Kruska,[1] Xin Zhang,[1] Xiaoxu Li,[1] Zhihan Hu,[2] Lin Shao,[2] Andrew M. Casella,[1] David J. Senor[1]

AFFLIATIONS

[1]Pacific Northwest National Laboratory, Richland, Washington 99352, USA
[2]Department of Nuclear Engineering, Texas A&M University, College Station, Texas 77843, USA

[a)]**Author to whom Correspondence should be addressed:** weilin.jiang@pnnl.gov

ABSTRACT

Defect accumulation and microstructural evolution during ion irradiation at elevated temperatures are governed by competing processes of defect production, driven by dose rate, and defect recovery, controlled by diffusion, interaction, and annihilation. This study investigates the effects of irradiation temperature and dose rate on microstructural evolution, deuterium retention, and lithium volatilization in γ-$LiAlO_2$ pellets subjected to sequential He^+ and D^+ ion irradiation. Experiments were performed to a total fluence of 3×10^{17} $(He^+ + D^+)/cm^2$ at 623, 673, 723, and 773 K with an average He^+ dose rate of 7.7×10^{-4} dpa/s, and to 2×10^{17} $(He^+ + D^+)/cm^2$ at 773 K with dose rates of 6.8×10^{-5}, 2.9×10^{-4}, and 7.3×10^{-4} dpa/s. At 623 K, the microstructure was dominated by cavities and fractures with no observable precipitate formation, while small precipitates emerged at 673 K. Increasing the irradiation temperature to 723–773 K promoted the formation of larger, faceted $LiAl_5O_8$ precipitates and surface amorphization, accompanied by pronounced lithium depletion and H-D isotopic exchange. At 773 K, medium and high dose rates produced an amorphized surface layer over a crystalline subsurface containing $LiAl_5O_8$ precipitates and blisters at the crystalline-amorphous interface, whereas low dose-rate irradiation preserved surface crystallinity with cavities distributed in the matrix, around precipitates, and along grain boundaries. Precipitate morphology was anisotropic with limited size dependence on dose rate. These results elucidate coupled effects of temperature and dose rate and demonstrate that sequential He^+ and D_2^+ irradiation at 773 K reproduces key microstructural features and H isotope behavior observed in neutron-irradiated γ-$LiAlO_2$ at 573 K.

I. INTRODUCTION

Gamma-phase lithium aluminate (γ-$LiAlO_2$) is a tritium-breeding ceramic for tritium production, with outstanding properties of low volumetric swelling[1] and high tritium retention during neutron irradiation.[2] Understanding the microstructural evolution and compositional changes in γ-$LiAlO_2$ under displacive irradiation is essential for predicting its performance in reactor environments. Sequential irradiation with He^+ and D_2^+ ions has been adopted to emulate the neutron-irradiation effects of helium and tritium production in γ-$LiAlO_2$, with deuterium serving as a non-radioactive surrogate for tritium. Previous studies[2-6] have demonstrated that sequential He^+ and D_2^+ ion irradiation successfully reproduces the microstructural features and gas transport behavior observed in neutron-irradiated γ-$LiAlO_2$ pellets. These include the formation of $LiAl_5O_8$ precipitates surrounded by cavities,[3] denuded zones along grain boundaries,[6] aggregation of cavities at boundaries,[6] isotopic exchange between mobile protium and trapped deuterium,[4] and lithium volatility.[7,8] The agreement with neutron irradiation results confirms the effectiveness of the ion-beam approach for investigating defect evolution and tritium behavior in lithium-containing ceramics.

Defect accumulation and microstructural evolution during ion irradiation are governed by two competing processes: (1) defect production, driven by dose rate, and (2) simultaneous defect recovery, controlled by defect diffusion, interaction, and annihilation at elevated temperatures. In addition to total dose, both irradiation temperature and dose rate play a critical role in governing microstructural evolution and compositional changes. For example, $LiAl_5O_8$ precipitates have been observed in γ-$LiAlO_2$ pellets irradiated in a thermalized fission neutron spectrum at 573 K,[2,6] whereas no precipitates appeared during sequential He^+ and D_2^+ ion irradiation at the same temperature.[5] At 773 K, however, precipitates formed during ion irradiation,[5,6,9] accompanied by microstructural features characteristic of neutron damage. The dose rate for ion irradiation is typically 2–4 orders of magnitude higher than that for neutron irradiation.[10] Such elevated rates can generate more complex and denser defect structures, producing deeper trapping sites for migrating atoms such as lithium and implanted gases. As a result, higher irradiation temperatures are often needed to activate atomic diffusion, promote defect recovery, and drive phase transformations comparable to those occurring under neutron exposure. In addition to microstructural differences, previous studies have revealed a significant influence of irradiation temperature on deuterium (and by inference, tritium) retention in γ-$LiAlO_2$.[2] As discussed in a separate study,[11] dose-rate effects arise only when defects, primarily point defects, from different damage cascades spatially overlap and either interact to form stable defect clusters (e.g., dislocation loops or voids) or annihilate through recombination with opposite defects. A physical model[11] predicts that both higher temperature and higher dose rate increase the probability of defect-defect interactions among subsequent damage cascades.

Recent investigations[6] examined the dependence of microstructural and compositional evolution on dose during sequential He^+ and D_2^+ irradiation at elevated temperature. Building on these results, the present study aims to evaluate the effects of irradiation temperature and dose rate on the microstructural evolution, deuterium retention, and lithium depletion in γ-$LiAlO_2$ pellets. These two parameters directly influence the competing processes of defect production and recovery that dictate microstructural evolution, compositional modification, and gas species redistribution during irradiation. By identifying the temperature shift required to emulate neutron irradiation conditions, this work provides new insights into the coupled mechanisms governing defect dynamics and gas transport in γ-$LiAlO_2$, offering a scientific basis for optimizing ion-irradiation protocols to better emulate reactor-relevant environments.

II. EXPERIMENTAL PROCEDURES

A. Sample preparation

Polycrystalline γ-$LiAlO_2$ pellet tubes were obtained from the TPBAR (Tritium-Producing Burnable Absorber Rod) pellet vendor. The tubes were sectioned tangentially to the inner and outer circular surfaces to produce rectangular specimens approximately 5 mm wide, 12 mm long, and 0.5 mm thick, each with two flat parallel faces. The slices were mounted on aluminum stubs using wax. All grinding was performed on a Struers 8-inch lapping wheel using Wendt Dunnington OS114 lapping oil. One-side polishing for ion irradiation was first conducted on a nylon cloth using Buehler MetaDi II 6 μm diamond paste with lapping oil. The specimens were then cleaned in an ultrasonic bath, rinsed, and blow-dried. Subsequent polishing was carried out using Buehler MetaDi II 1 μm diamond paste with lapping oil following the same procedure. The samples were then placed on a Struers vibratory polisher for ~16 h. Final polishing of the front surface of each slice was performed using colloidal silica. The polished samples were subsequently baked in air at 773 K for 4 h. Heating and cooling were carefully controlled at ramp rates of 3.9 K/min and -0.5 K/min, respectively, to prevent quenching-induced cracking or thermal stress. After baking, the samples were stored in a dry helium atmosphere.

B. SRIM simulation and ion irradiation

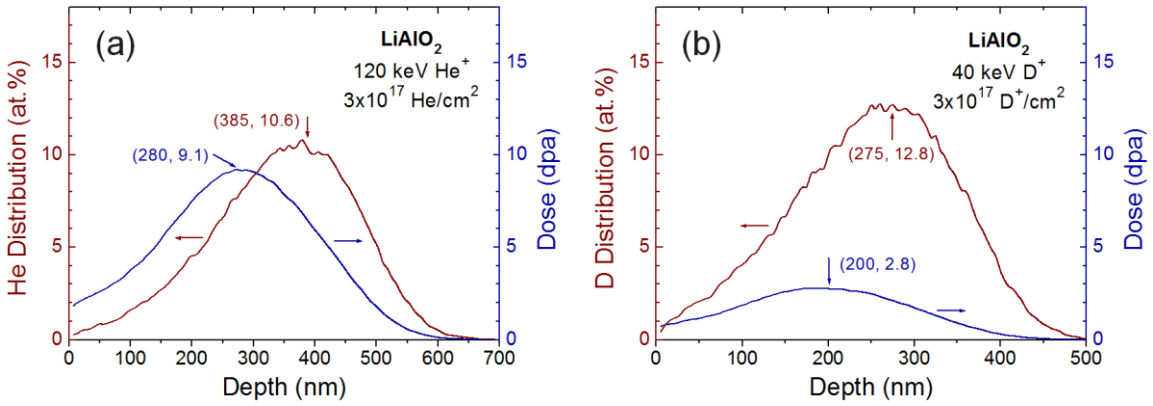

FIG. 1. Depth profiles of the atomic percentage and dose from SRIM13 simulations for (a) 120 keV He^+ and (b) 40 keV D^+ ion irradiations of γ-$LiAlO_2$ at 60° off normal to a fluence of 3×10^{17} ions/cm^2.

Thermal neutron irradiation effects in γ-$LiAlO_2$ are expected to be effectively emulated through irradiation with energetic He^+ and T^+ ions to equal fluences that yield comparable displacement damage. Both ions lose energy primarily through electronic interactions in γ-$LiAlO_2$ at high energies, while nuclear stopping, responsible for producing lattice damage, becomes dominant below ~15 keV/amu for T^+ and ~25 keV/amu for He^+. The maximum nuclear stopping powers occur at ~0.225 keV for T^+ and ~0.5 keV for He^+, respectively. In this study, D^+ ions were used as a nonradioactive surrogate for T^+ ions. Because the majority of displacement damage arises from the heavier He^+ ions and the potential He roles in cavity formation,[12] sequential irradiation with He^+ followed by D^+ ions was designed to ensure that the implanted D concentration peak spatially overlaps with the He^+-induced damage peak, thereby enabling D trapping at pre-existing He-induced defect sites.

Table I. SRIM simulation results for He^+ and D^+ ion irradiations of γ-$LiAlO_2$ pellets.

3×10^{17} ions/cm^2 60° off	Damage Peak Depth (nm)	Peak Dose (dpa)	Profile Peak Depth (nm)	Peak Concentration (at. %)
120 keV He^+	280	9.1	385	10.6
40 keV D^+	200	2.8	275	12.8

Table II. Ion irradiation conditions for γ-$LiAlO_2$ pellets.

	Ion Species	Energy (keV)	Fluence (ions/cm^2)	Temperature (K)	Dose Rate (dpa/s)
Sequence 1	He^+	120	3×10^{17}	623, 673 723, 773	7.7×10^{-4}
Sequence 2	D_2^+	80	3×10^{17}	623, 673 723, 773	
Sequence 1	He^+	120	2×10^{17}	773	6.8×10^{-5}, 2.9×10^{-4},
Sequence 2	D_2^+	80	2×10^{17}	773	7.3×10^{-4}

80 keV D_2^+ molecular ions are equivalent to 40 keV D^+ ions for irradiation.

To guide the experimental design, the distributions of displaced atoms and implanted species were simulated using SRIM13 (Stopping and Range of Ions in Matter, version 2013).[13] The calculations were performed for 120 keV He^+ and 40 keV D^+ ions incident at 60° relative to the surface normal into γ-$LiAlO_2$ (density 2.615 g/cm^3). The "monolayer collision step/surface sputtering" option was used to minimize surface artifacts from energetic light ions. Threshold displacement energies were adopted from molecular dynamics simulations as E_a(Li) = 22 eV, E_a(Al) = 84 eV, and E_a(O) = 37 eV,[14] with surface binding energies set equal to the corresponding threshold values. The calculated depth profiles of the displaced atoms and implanted He and D in γ-$LiAlO_2$ for a total fluence of 3×10^{17} ions/cm^2 are shown in Fig. 1, and the key parameters are summarized in Table I. For 120 keV He^+ irradiation, the peak dose reaches 9.1 dpa at a depth of ~280 nm, while the peak He concentration is 10.6 at.% at ~385 nm. This He level is equivalent to a ^{6}Li burnup of ~42 at.% in γ-$^6LiAlO_2$ irradiated under a thermalized fission neutron spectrum.[2] For 40 keV D^+ irradiation, the peak dose is 2.8 dpa at 200 nm, and the peak D concentration is 12.8 at.% at 275 nm. The combined maximum dose of 11.4 dpa occurs at 255 nm. The D implantation profile overlaps well with the He-induced damage region, providing the desired configuration for studying D trapping at He-stabilized defect structures. It should be noted that previous reports[15,16] have proposed using the "full damage cascade" option with adjusted parameters in SRIM13. In the present study, dpa doses were calculated using the monolayer collision step option, which yields values nearly

identical to those from the full cascade option and approximately twice as high as those from the quick calculation option. However, since these dpa values in this study are used exclusively for relative comparisons of damage levels, their absolute magnitudes do not affect the interpretation of the results.

Sequential ion irradiation experiments were conducted using a 140 kV ion accelerator equipped with a magnetic rastering system. Irradiation was performed at an incident angle of 60° to the surface normal using 120 keV He^+ and then 80 keV D_2^+ ions. The use of a D_2^+ molecular beam enabled a higher D^+ ion flux. The molecular ion beam provides a significantly higher current, and upon entering the target, each 80 keV D_2^+ ion dissociates into two 40 keV D^+ ions, thereby maintaining equivalent implantation conditions while doubling the ion flux. The combination of relatively low ion energies and a tilted geometry was chosen to facilitate subsequent depth profiling of implanted species and damage distributions. To ensure uniform irradiation, both He^+ and D_2^+ beams were rastered over the sample surface. The beam current was manually checked every ~15 minutes, and average values were used to calculate fluence; however, the total ion fluence carries an uncertainty of ~10%. Samples were heated to the targeted temperature using a filament positioned behind a copper sample holder prior to irradiation. One set of samples were irradiated to a fluence of 3×10^{17} $(He^+ + D^+)/cm^2$ at 623, 673, 723 and 773 K. The average He^+ and D_2^+ beam fluxes were 2.5×10^{13} $(He^+/cm^2)/s$ and 2.9×10^{13} $(D^+/cm^2)/s$, corresponding to peak dose rates of 7.7×10^{-4} and 2.9×10^{-4} dpa/s, respectively, as summarized in Table II. The other set of samples were irradiated at a fixed temperature of 773 K to a total fluence of 2×10^{17} $(He^+ + D^+)/cm^2$ under three dose rates: 6.8×10^{-5}, 2.9×10^{-4}, and 7.3×10^{-4} dpa/s, as also listed in Table II. The corresponding irradiation durations were 31, 7.1, and 2.9 hours, respectively, while maintaining same He^+ and D^+ ion fluxes in all cases. After irradiation, the γ-$LiAlO_2$ pellets were sealed in Ar-filled glass vials and secured with tape to minimize exposure to air and prevent moisture-induced degradation prior to characterization.

C. Sample characterization

Cross-sectional scanning transmission electron microscopy (STEM) specimens were prepared from the irradiated γ-$LiAlO_2$ pellets using FEI Quanta 3D and Helios 600 Nanolab dual-beam focused ion beam (FIB) microscopes. To protect the specimen surface during milling, regions of interest were capped with ~300 nm of electron-beam–deposited Pt followed by ~4 μm of ion-beam-deposited carbon. Site-specific lamellae were extracted using a standard Ga^+ ion-beam lift-out procedure and mounted onto Cu support grids. Thinning was performed by gradually reducing the Ga^+ ion beam energy from 30 to 16, 8, and 5 kV while sequentially lowering the stage tilt from ±5° relative to 52°. When the lamellae reached an approximate thickness of 100 nm, final polishing was carried out at 2 kV with the stage tilted to 59° (±7° from 52°) to achieve electron transparency and minimize ion-beam-induced damage.

The specimens were examined using a ThermoFisher Scientific aberration-corrected Spectra Ultra STEM operated at 300 kV. High-angle annular dark-field (HAADF) STEM imaging was employed to characterize the irradiated microstructures, providing atomic number (Z)-contrast sensitivity to reveal compositional and structural variations across the irradiated regions. To mitigate electron-beam-induced damage and minimize sample heating, low-dose imaging conditions were used, with a beam current of 20 pA, a dwell time of ~1 μs per pixel, and frame averaging over ~20 sequentially acquired, spatially overlapping images. This acquisition strategy improved the signal-to-noise ratio while preserving microstructural integrity.

Chemical depth profiling of H, D, Li, and Al in the irradiated γ-$LiAlO_2$ pellets was performed using a time-of-flight secondary ion mass spectrometry (ToF-SIMS) instrument (IONTOF GmbH, Münster, Germany) operated at room temperature. A 2.0 keV Cs^+ beam (~59 nA) rastered over a 200 × 200 μm^2 area was used as the sputtering beam, while a pulsed 25 keV Bi^+ beam (~0.75 pA, ~5 μm spot size, 10 kHz repetition rate) rastered over a 50 × 50 μm^2 area centered within the sputtered crater for analysis. Negative secondary ions were collected to enhance the detection sensitivity to the low-concentration implanted deuterium and migrating protonium from the environment. The measurements were performed in non-interlaced mode with a cycle consisting of 10.0 s sputtering, a 2.0 s pause, and 3.28 s data acquisition. Charge compensation was achieved using a low-energy (10 eV) electron flood gun. In addition, a ~15 nm Au film was deposited on the backside of the samples to further mitigate charging effects and enhance signal intensity.[17] This dual-beam configuration provided high depth resolution while minimizing charging and topographical artifacts, enabling reliable determination of isotope distributions and elemental depth profiles in γ-$LiAlO_2$.

III. RESULTS AND DISCUSSION

A. Temperature effects

1. Microstructural evolution

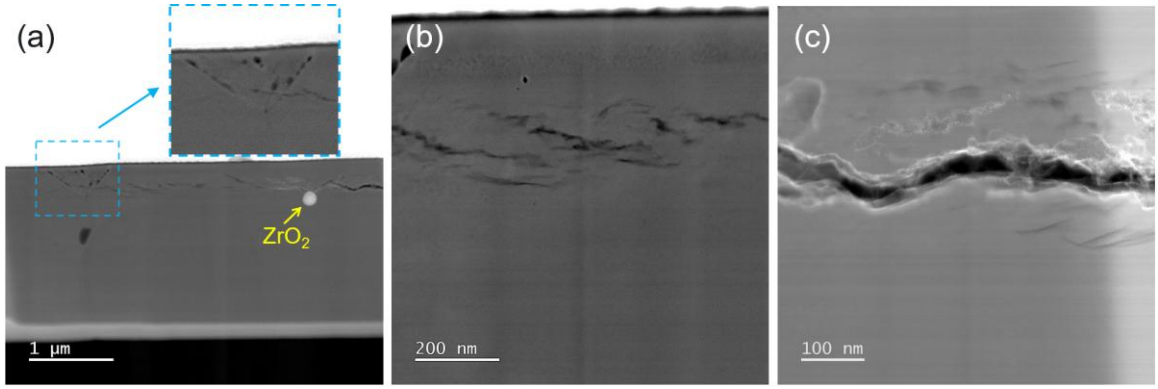

FIG. 2. STEM micrographs showing the microstructure of a γ-$LiAlO_2$ pallet irradiated at 623 K to 3×10^{17} $(He^+ + D^+)/cm^2$ at (a) low, (b) medium, and (c) high magnifications.

Figure 2 presents HAADF-STEM images at multiple magnifications exhibiting the microstructure of a γ-$LiAlO_2$ pellet irradiated to a fluence of 3×10^{17} $(He^+ + D^+)/cm^2$ at 623 K, with an average He^+ dose rate of 7.7×10^{-4} dpa/s. Distinct fractures appear around the depth of the helium concentration peak. A similar microstructure was observed in a γ-$LiAlO_2$ pellet irradiated to 2×10^{17} $(He^+ + D^+)/cm^2$ at 573 K.[5] Cavities are also observed to aggregate preferentially along grain boundaries [Fig. 2(a)], formed through the interaction of irradiation-induced vacancies with implanted helium atoms, likely in combination with deuterium. The bright contrast seen in Fig. 2(a) corresponds to a pre-existing ZrO_2 impurity particle (introduced during powder milling) within the γ-$LiAlO_2$ matrix. However, second-phase precipitates were not formed within the irradiated microstructure. The lack of new precipitates suggests that 623 K remains

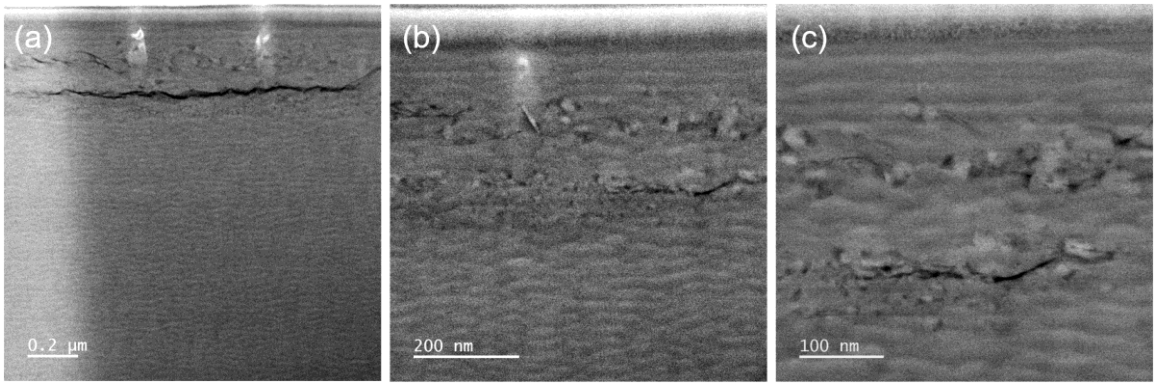

FIG. 3. STEM micrographs showing the microstructure of a γ-$LiAlO_2$ pallet irradiated at 673 K to 3×10^{17} $(He^{+}+D^{+})/cm^2$ at (a) low, (b) medium, and (c) high magnifications.

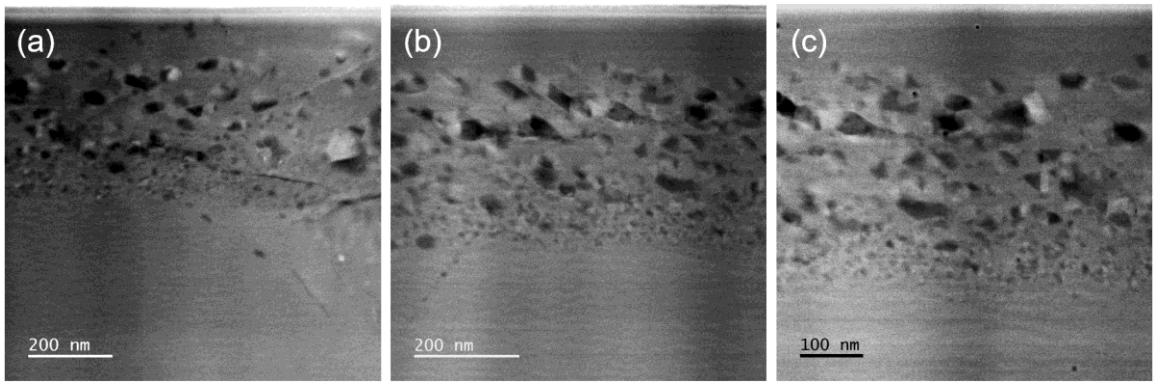

FIG. 4. STEM micrographs showing the microstructure of a γ-$LiAlO_2$ pallet irradiated at 723 K to 3×10^{17} $(He^{+}+D^{+})/cm^2$ at (a) low, (b) medium, and (c) high magnifications.

too low to drive phase transformation, whereas the observed cavities and fractures indicate active gas-vacancy clustering and growth at this temperature.

For the sample irradiated at 673 K, more significant microstructural evolution is observed, as shown in Fig. 3. An amorphous surface layer ~70 nm thick forms, likely as a result of radiolysis under energetic He^{+} and D^{+} irradiation. Radiolysis itself shows only weak temperature dependence during the initial excitation, ionization, and bond-breaking events, which are primarily governed by energy deposition. Although increasing temperature raises atomic vibrational energy and vibration amplitude, slightly enhancing the probability of bond rupture, this effect is secondary. In contrast, the observable consequences of radiolysis are strongly temperature dependent because defect diffusion, clustering, recombination, and chemical reactions are all thermally activated. In addition to the formation of longer fractures, the damage peak region exhibits the emergence of small cavities and fine precipitates, as shown in Figs. 3(b) and 3(c). The striation contrast in Fig. 3 is recognized as an artifact from FIB processing, as it extends well beyond the irradiated zone. The observed microstructure indicates that the critical temperature for solid-state precipitate nucleation under the present ion fluxes (2.5×10^{13} $He^{+}/cm^2/s$ and 2.9×10^{13} $D^{+}/cm^2/s$) lies between 623 K and 673 K. The coexistence of cavities, fractures, and fine

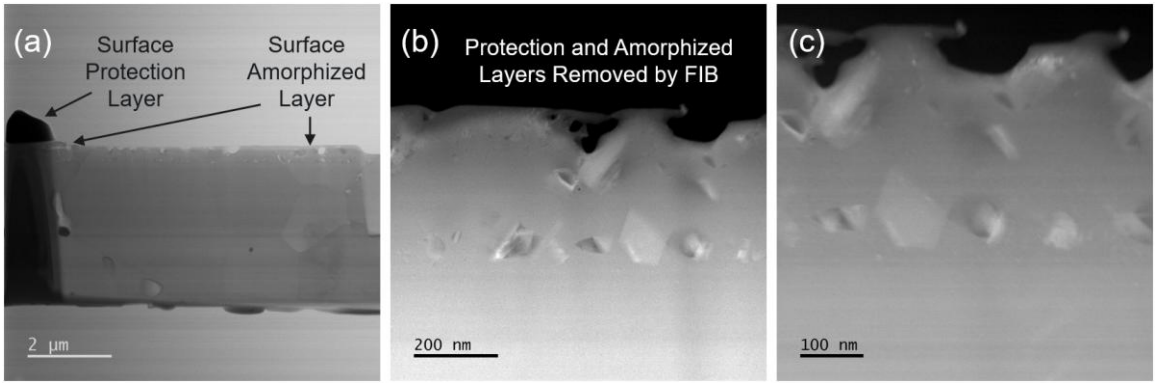

FIG. 5. TEM/STEM micrographs showing the microstructure of a γ-$LiAlO_2$ pallet irradiated at 773 K to 3×10^{17} $(He^+ + D^+)/cm^2$ at (a) low, (b) medium, and (c) high magnifications.

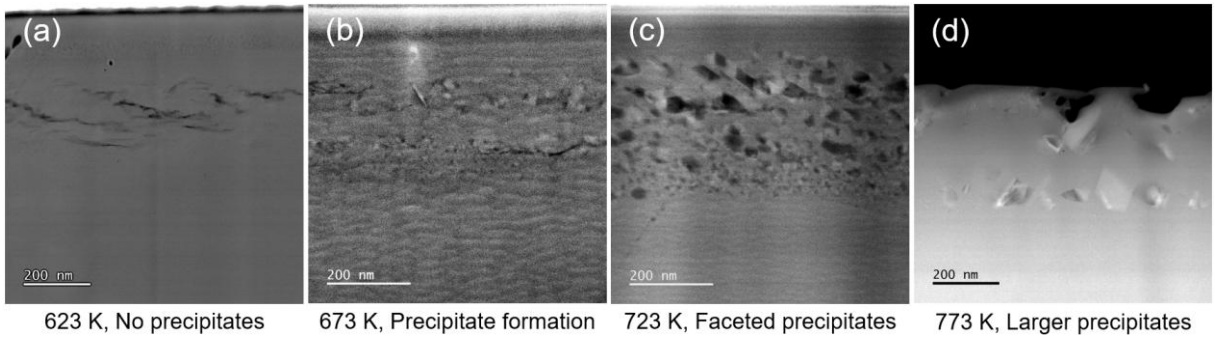

FIG. 6. STEM micrographs showing the microstructures of γ-$LiAlO_2$ pallets irradiated to 3×10^{17} $(He^+ + D^+)/cm^2$ at (a) 623 K, (b) 673 K, (c) 723 K, and (d) 773 K.

precipitates points to increased atomic mobility and chemical segregation driven by irradiation-enhanced diffusion processes.

At 723 K, an amorphized surface layer persists [Fig. 4], and the irradiation-induced cavities and precipitates undergo coarsening. Compared to those formed at 673 K, the precipitates at 723 K are larger, well-faceted, and distributed over a broader depth range (approximately 120–410 nm). This trend reflects the temperature-dependent enhancement of defect mobility, which accelerates both precipitate growth and ripening. The dark-contrast feature in Fig. 4 corresponds to cavities, some of which extend to depths of ~600 nm below the surface along grain boundaries, reflecting the faster diffusion pathways provided by these boundaries. While small fractures remain visible, extended fractures are absent. This reduction in fracture severity may result from faster diffusion of vacancies and implanted gases at higher temperatures, which facilitates gas release and promotes defect recovery during irradiation.

At 773 K, the microstructure becomes even more evolved, as shown in Fig. 5. An amorphous surface layer remains visible beneath the protective cap [partially retained in the upper left corner of Fig. 5(a) and a portion on the right]. Large, faceted precipitates up to ~200 nm in size develop around the damage peak. Some precipitates are surrounded by cavities, consistent with previous reports in which the precipitates were identified as nonstoichiometric $LiAl_5O_8$.[3,6,9] Notably, microstructural fractures are not observed at the He concentration peak, probably due to more significant release of gaseous species.

Figure 6 compares the evolution of γ-$LiAlO_2$ microstructures irradiated to 3×10^{17} $(He^+ + D^+)/cm^2$ over the temperature range 623–773 K. At 623 K, no solid precipitates form; instead, cavities and fractures develop at the He concentration peak. At 673 K, small precipitates emerge alongside surface amorphization, fractures, and cavities, marking the transition for precipitate nucleation and growth. At 723 K, faceted precipitates become more abundant and larger, with extended cavity networks and a persistent amorphous surface layer. At 773 K, large, faceted precipitates dominate around the damage peak. Overall, the observed microstructural evolution demonstrates a clear temperature-dependent transition from a cavity-dominated microstructure to a precipitate-dominated one, accompanied by surface amorphization.

2. Deuterium retention and lithium depletion

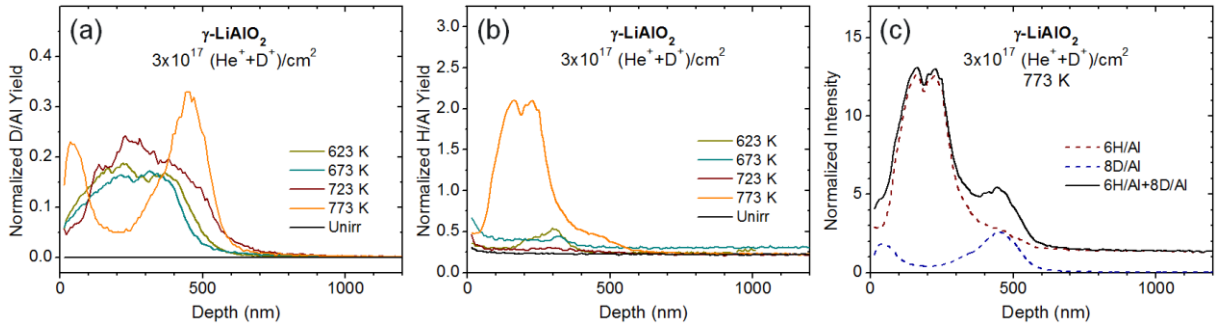

FIG. 7. ToF-SIMS depth profiles of normalized (a) D/Al and (b) H/Al yields in γ-$LiAlO_2$ pellets irradiated to 3×10^{17} $(He^+ + D^+)/cm^2$ at various temperatures, along with those in an unirradiated pellet. (c) Relative concentrations of H, D, and their sum in the pellet irradiated at 773 K.

Figure 7 presents the ToF-SIMS depth profiles of deuterium and hydrogen, expressed as normalized D/Al and H/Al yield ratios, in γ-$LiAlO_2$ pellets irradiated to a fluence of 3×10^{17} $(He^+ + D^+)/cm^2$ at temperatures ranging from 623 to 773 K. The corresponding profiles for an unirradiated pellet are also included for comparison. Throughout the analysis, the Al yield is assumed to remain constant with depth, as the Al matrix signal is relatively insensitive to the irradiation-induced compositional variations and serves as a normalization reference. As expected, the unirradiated sample exhibits nearly zero D/Al and very low H/Al yields. It is important to note that ToF-SIMS selectively detects atomic deuterium trapped within the microstructure, whereas molecular D_2 gas confined in cavities can escape immediately into the vacuum upon sputtering-induced rupture and may therefore not be effectively detected.

At 773 K, the D depth profile exhibits a distinct double-peak structure [Fig. 7(a)], accompanied by a corresponding H peak in the same depth region [Fig. 7(b)]. This correlated feature suggests an isotopic exchange process between migrating H and trapped D during irradiation. Such behavior is consistent with our previous ion-irradiation studies on γ-$LiAlO_2$,[4] in which isotopic exchange occurred under similar conditions. Isotopic exchange represents a reversible chemical reaction between isotopic species, where isotopes are exchanged without a net energy input. This process can alter the apparent depth distributions of H isotopes and has been reported to enhance tritium release in neutron-irradiated lithium ceramics through H-T isotopic exchange mechanisms.[18] In the present study, the emergence of the D double-peak structure at 773 K implies that the exchange reaction becomes thermally activated above a certain temperature threshold, enabling redistribution of H and D in the near-surface region.

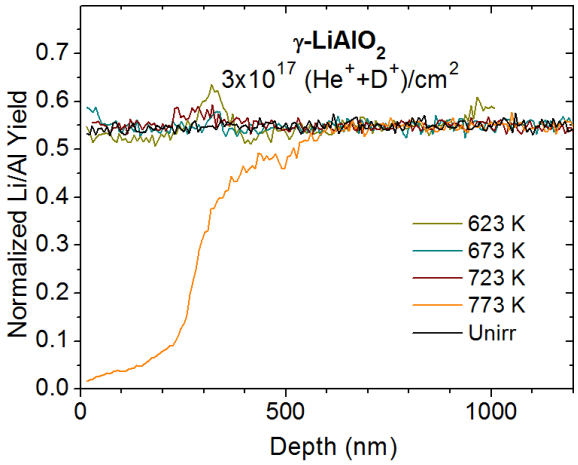

FIG. 8. ToF-SIMS depth profiles of normalized Li/Al yields in γ-$LiAlO_2$ pellets irradiated to 3×10^{17} $(He^+ + D^+)/cm^2$ at various temperatures, along with those in an unirradiated pellet.

Fig 7(c) shows the relative concentrations of H, D, and their sum in the pellet irradiated at 773 K. These values were estimated using the ToF-SIMS relative sensitivity factors (RSFs) for protium (6×10^{21} cm^{-3}) and deuterium (8×10^{21} cm^{-3}) determined for GaAs.[19] The results suggest substantially greater retention of protium within the irradiated region of the sample. The low protium background observed at depths greater than 600 nm is likely attributable to the absorption of H-containing species from the ultrahigh-vacuum environment onto the freshly sputtered surface prior to analysis during the dual-beam ToF-SIMS measurement cycle.

At 623 K, a broad, low-intensity H peak appears at ~300 nm, as shown in Fig. 7(b). This peak becomes broader at 673 K and nearly disappears at 723 K before evolving into a pronounced peak at ~200 nm. SRIM simulations (Fig. 1) indicate that the He damage peak is located at ~280 nm, whereas the D damage peak is centered at ~200 nm. The H enrichment near ~300 nm observed at 623 K is attributed to trapping of diffusing environmental H at irradiation-induced defects associated with the He-damaged region. At this temperature, vacancies and small vacancy clusters remain effective trapping sites. With increasing temperature to 673 and 723 K, thermally activated detrapping and enhanced H mobility reduce H retention at these defect sites, leading to a decrease in H concentration in the He damage region. These observations indicate that isotopic exchange is either kinetically limited or inactive at 723 K and below. At 773 K, however, thermally activated diffusion and exchange processes become dominant. As a result, H redistribution is increasingly governed by isotopic exchange with trapped D near the D implantation peak (~200 nm), leading to the pronounced H signal observed in that region.

Figure 8 shows the normalized Li/Al yield ratios as a function of depth for the same γ-$LiAlO_2$ pellets shown in Fig. 7. The unirradiated sample serves as a baseline, exhibiting a depth-independent Li/Al ratio, as expected. In contrast, pronounced Li depletion is observed near the surface of the pellet irradiated at 773 K, extending to a depth of ~200 nm. The apparent Li depletion is attributed to thermally enhanced diffusion of Li interstitials toward the surface, where Li species may be preferentially released through volatile metal or Li–O–H complexes. Surface sputtering may also contribute. The observed trend is consistent with previous ToF-SIMS analyses of γ-$LiAlO_2$ pellets irradiated at 773 K.[5,7] The extent of Li loss depends on grain size, porosity, surface preparation, and subtle variations in irradiation conditions such as residual gas environment. Notably, the Li-depleted region spatially coincides with the amorphized

surface layer in Fig. 5, where a D valley and H peak are observed in Fig. 7. Radiolysis-induced bond rupture contributes to structural destabilization and amorphization, followed by significant Li out-diffusion and release. Previous compositional analysis of irradiated γ-$LiAlO_2$ has shown[5] that regions containing $LiAl_5O_8$ precipitates exhibit a step-like decrease in Li concentration relative to the surrounding γ-$LiAlO_2$ matrix, indicating Li redistribution during precipitate formation. Under irradiation conditions the Li atoms expelled from the precipitates during the compositional partitioning exhibit high mobility and can diffuse toward the surface. Li atoms reaching the surface can be removed through evaporation and/or sputtering processes.

In contrast, at lower irradiation temperatures (≤ 723 K), no measurable Li loss is detected within the ToF-SIMS resolution limits, suggesting that Li diffusion and volatilization from γ-$LiAlO_2$ under He^+ and D^+ ion irradiation are strongly suppressed under these conditions. As small variations in Li concentration are challenging to detect within the high Li background of the irradiated pellet, minor Li loss under lower-temperature irradiation conditions cannot be definitively excluded.

B. Dose rate effects at 773 K

1. Crystal structure of tetragonal γ-$LiAlO_2$

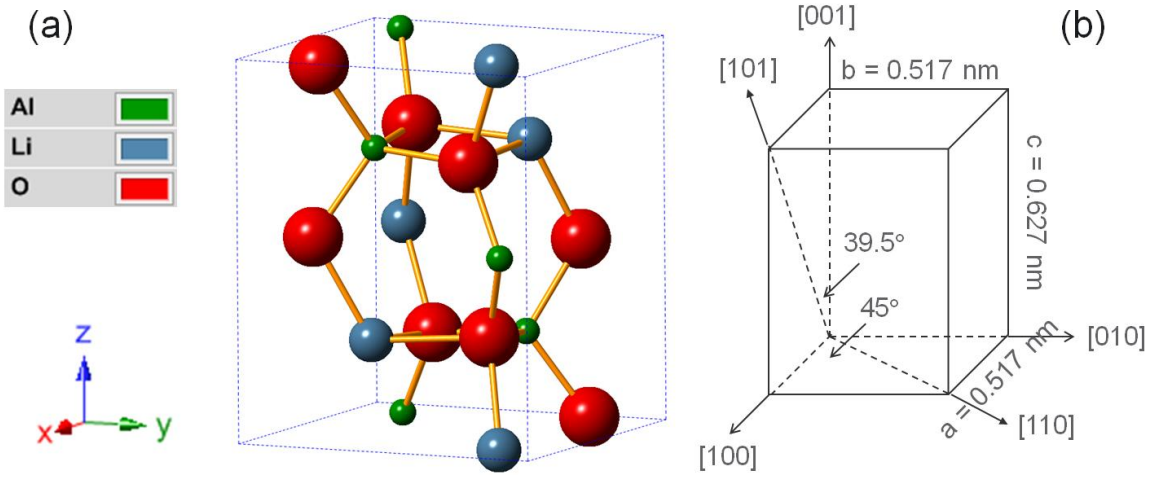

FIG. 9. (a) Unit cell of the tetragonal γ-$LiAlO_2$ crystal structure, and (b) schematic for the unit cell showing crystallographic axes.

Figure 9(a) illustrates the unit cell of γ-$LiAlO_2$, generated using the commercial visualization software Crystal Maker. The γ-$LiAlO_2$ phase crystallizes in the tetragonal crystal system with space group $P4_12_12$ (No. 92). At room temperature, its lattice parameters are $a = b = 0.51687$ nm and $c = 0.62679$ nm. The corresponding theoretical mass density is 2.615 g/cm^3, which yields an atomic density of 9.555×10^{22} at./cm^3. The γ-$LiAlO_2$ structure consists of corner-sharing AlO_4 and LiO_4 tetrahedra arranged in alternating layers along the *c*-axis, forming a three-dimensional network stabilized by strong ionic-covalent bonding between Li^+, Al^{3+}, and O^{2-} ions. The symmetry elements of the γ-$LiAlO_2$ crystal are defined by a fourfold screw rotation along the [001] axis and twofold rotations about the [100], [010], and [110] axes. Therefore, the [100] and [001] directions are crystallographically nonequivalent, as are the

[110] and [101] directions. Fig. 9(b) schematically illustrates the angular relationships between several major crystallographic directions: a 45° angle between [100] and [110], and a 39.5° angle between [001] and [101]. These relationships are important for interpreting TEM diffraction patterns.

In the present study, the γ-$LiAlO_2$ specimens were examined using a STEM microscope equipped with a double-tilt goniometer stage capable of a maximum specimen tilt of approximately ±30°. This limitation constrains accessible zone axes to low-index orientations such as [100] (and possibly [110]) or [001] (and possibly [101]), depending on the initial orientation of the lift-out lamella. Because of this geometrical constraint and the near-tetragonal symmetry, there is a 50% probability that a FIB lift-out specimen will be aligned along either the [100] or [001] zone axis. Identification of the zone axis was achieved through selected-area electron diffraction (SAED) pattern analysis.

2. Microstructural features and precipitate characteristics

a. High dose-rate case

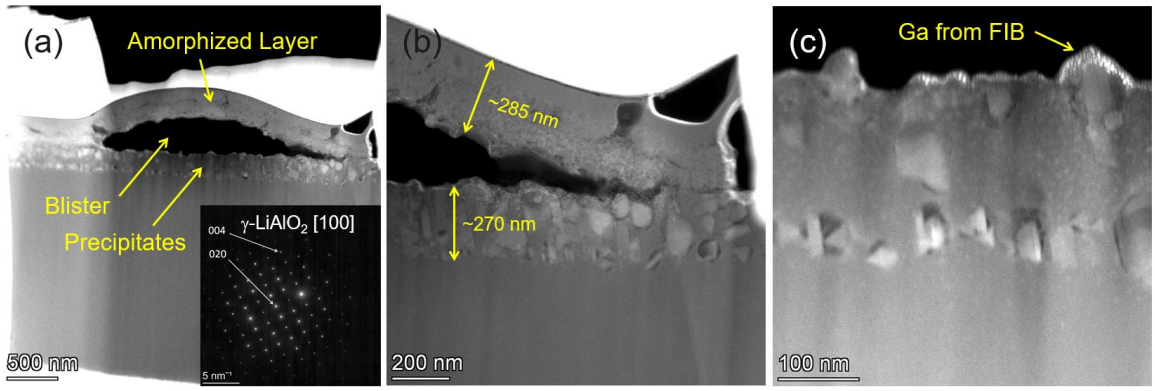

FIG. 10. STEM micrographs showing the microstructure of a [100]-oriented γ-$LiAlO_2$ pallet irradiated to 2×10^{17} $(He^+ + D^+)/cm^2$ at 773 K with a high dose rate of 7.3×10^{-4} dpa/s, acquired at (a) low, (b) medium, and (c) high magnifications.

A crystalline γ-$LiAlO_2$ grain, several micrometers in size, was examined from the FIB-prepared cross-sectional specimen irradiated to a combined fluence of 2×10^{17} $(He^+ + D^+)/cm^2$ at 773 K with a high dose rate of 7.3×10^{-4} dpa/s. The grain was manually oriented in the TEM with respect to the analytical electron beam. The corresponding selected-area electron diffraction (SAED) pattern is shown in the inset of Fig. 10(a). The brightest spot corresponds to the transmitted (direct) beam, while the surrounding bright spots arise from Bragg diffraction of the crystalline lattice of γ-$LiAlO_2$. According to the simulated diffraction pattern (not shown), the (004) and (020) reflections are expected. In contrast, reflections such as (001), (002), (003), and (010) are systematically forbidden for a perfect γ-$LiAlO_2$ crystal because of symmetry-imposed extinction conditions. The presence of these "forbidden" reflections in Fig. 10(a) is attributed to defect-induced lattice distortions that locally break the ideal symmetry, resulting in incomplete cancellation of the diffracted intensity. The intensities of these reflections can depend on several factors, including the degree of crystallographic perfection, local strain, defect density, specimen thickness, and beam alignment or illumination conditions. These additional diffraction spots, however, do not suggest the formation of secondary phases or new structural features.

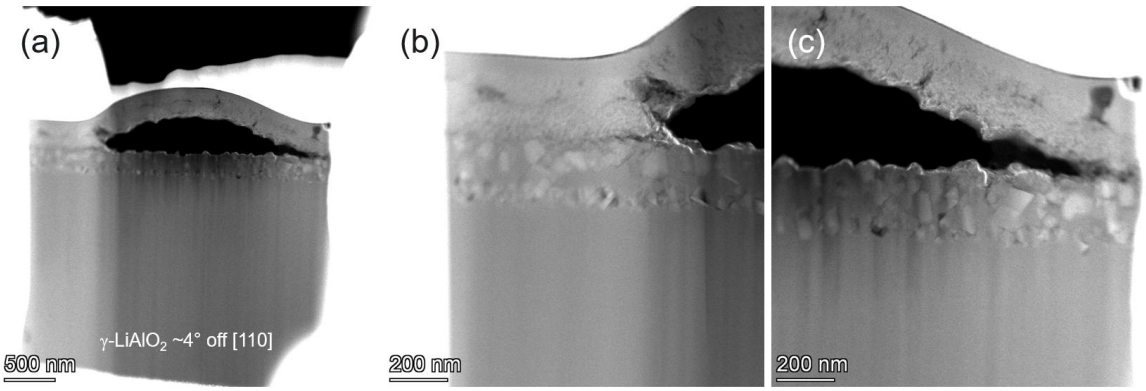

FIG. 11. STEM micrographs showing the microstructure of a nearly [110]-oriented γ-$LiAlO_2$ pallet irradiated to 2×10^{17} $(He^+ + D^+)/cm^2$ at 773 K with a high dose rate of 7.3×10^{-4} dpa/s, acquired at (a) low, (b) and (c) medium magnifications.

By analyzing the *d*-spacings of the (004) and (020) reflections, the γ-$LiAlO_2$ grain was determined to be oriented along the [100] zone axis. Fig. 10 presents the microstructural features observed in this irradiated grain. A prominent surface blister, approximately 1.7 μm in length, is evident. The uppermost layer of the blistered region is fully amorphized, as indicated by diffuse contrast (not shown). The result suggests that radiation-induced decomposition associated with electronic stopping processes in the near-surface region may play a dominant role in the observed amorphization. SRIM simulations indicate that, for both 120 keV He^+ and 40 keV D^+ ion irradiations, the electronic stopping power near the surface of γ-$LiAlO_2$ is significantly higher than the nuclear stopping power. Under these conditions, electronic energy deposition, where electronic excitations and ionization dominate over elastic atomic displacements, can induce ionization, chemical bond breaking, and radiolysis in the near-surface region. Similar near-surface amorphization driven by electronic energy loss has been reported in lithium silicates such as Li_2SiO_3 and Li_4SiO_4.[20] At present, it remains unclear whether the amorphous layer formed during the initial He^+ irradiation or during the subsequent D_2^+ exposure, as both irradiation steps can contribute to amorphization and gas pressurization that ultimately drives blister formation at elevated temperatures. Ongoing work aims to clarify the relative contributions of these irradiation stages, and the results will be reported in a future study.

Beneath the amorphous surface layer lies a crystalline region densely populated with nanoscale precipitates, previously identified[5,9] as nonstoichiometric $LiAl_5O_8$, as shown in Fig. 10. In this region, displacement damage generated by ballistic atomic collisions becomes the dominant irradiation process. Because irradiation in this study was conducted at elevated temperatures between 573 and 773 K, irradiation-induced point defects are sufficiently mobile to recombine. This dynamic recovery process substantially reduces the accumulation of stable defect clusters, thereby suppressing the buildup of defect concentrations required for amorphization. Consequently, the crystalline structure is preserved despite the higher dpa levels relative to the near-surface region.

The formation of the cubic $LiAl_5O_8$ precipitates can be interpreted as a consequence of Li redistribution and the resulting Li-deficient local environment. Compared with γ-$LiAlO_2$, $LiAl_5O_8$ contains less Li and can therefore represent a thermodynamically favored phase under Li-deficient conditions. The precipitates observed in irradiated γ-$LiAlO_2$ are not uniformly distributed throughout the

irradiated region but are instead confined to a relatively narrow depth range near the damage peak. An approximate areal number density can be estimated from the available TEM images. Based on the number of precipitates visible in Fig. 10(c), the areal density is on the order of ~1.5×10^{10} precipitates/cm^2. This value should be regarded as an order-of-magnitude estimate, given the limited number of analyzed images and possible projection effects. The precipitates are typically several to several tens of nanometers in diameter, corresponding to approximate precipitate volumes on the order of ~10^2–10^4 nm^3 assuming roughly equiaxed shapes. These estimates provide a general indication of the precipitate population but should not be interpreted as precise quantitative measurements. Although large $LiAl_5O_8$ precipitates extending toward the amorphized surface region have been reported previously,[5] there has been no clear evidence for the nucleation and growth of such precipitates directly within the amorphous layer.

The blister interface clearly delineates the crystalline-amorphous regions. The curvature of the blister suggests significant internal pressurization, most likely from the accumulation and coalescence of implanted gases (He and D_2) at the amorphous-crystalline interface. On the [100] orientation projection, the amorphized layer and the precipitate-containing region measured ~285 and ~270 nm in thickness, respectively. Minor Ga contamination introduced during FIB milling is also evident in Fig. 10(c), though its influence on the observed microstructure is minimal due to its limited spatial extent.

The individual blisters in the irradiated γ-$LiAlO_2$ pellet (2×10^{17} (He^++D^+)/cm^2 at 773 K) are not clearly resolved in the plan-view low-mag SEM images (not shown) due to the relatively low surface contrast under the imaging conditions used during lamella preparation. The TEM lift-out regions were selected essentially randomly, without prior knowledge of whether a blister was present. Characterization performed in a separate study using atomic force microscopy (AFM) on a γ-$LiAlO_2$ pellet irradiated under the same conditions revealed a distribution of surface blisters across the irradiated surface, with an average blister size below ~1 μm (data not shown). In contrast, TEM examinations did not reveal large blister formation in samples irradiated at temperatures below 773 K, and no visible blistering was detected in samples irradiated at lower dose rates within the investigated range. These observations suggest that blister formation in γ-$LiAlO_2$ is strongly temperature dependent, likely requiring sufficient defect mobility and gas diffusion to enable cavity growth and coalescence into near-surface blisters. A systematic investigation of blister size distribution and number density as a function of irradiation conditions is beyond the scope of the present study.

To further examine the three-dimensional morphology of irradiation-induced features, the same grain was tilted toward the [110] zone axis. Due to the limited rotation range of the TEM goniometer (±30°), the orientation was slightly misaligned by ~4° from the exact [110] direction; however, the small deviation does not significantly affect the appearance of microstructural features. Fig. 11 shows STEM images obtained near the [110] orientation, revealing microstructures similar to those seen along [100], including the surface blister, amorphized region, and precipitate-rich crystalline layer.

b. Medium dose-rate case

A similar alignment procedure was performed on a crystalline γ-$LiAlO_2$ grain extracted from the FIB-prepared specimen irradiated to a combined fluence of 2×10^{17} (He^++D^+)/cm^2 at 773 K under a medium dose rate of 2.9×10^{-4} dpa/s. The SAED pattern obtained from this grain is shown in the inset of Fig. 12(a), confirming that the grain was oriented along the [001] zone axis. In the tetragonal γ-$LiAlO_2$ structure, the [001] and [100] directions are orthogonal but crystallographically inequivalent, as discussed above.

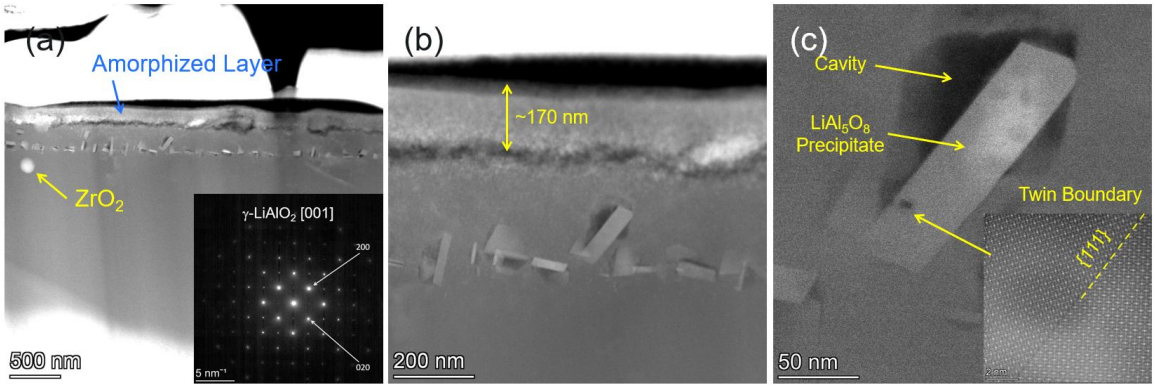

FIG. 12. STEM micrographs showing the microstructure of a [001]-oriented γ-$LiAlO_2$ pallet irradiated to 2×10^{17} $(He^+ + D^+)/cm^2$ at 773 K with a medium dose rate of 2.9×10^{-4} dpa/s, acquired at (a) low, (b) medium, and (c) high magnifications.

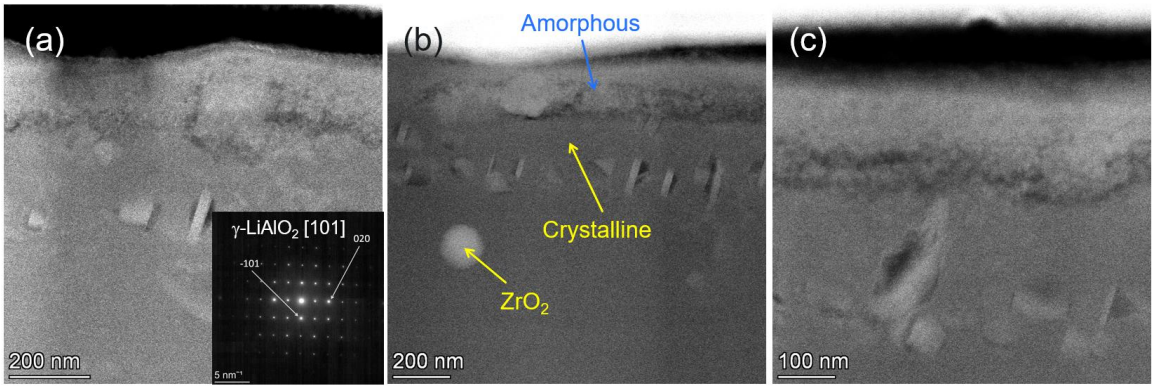

FIG. 13. STEM micrographs showing the microstructure of a [101]-oriented γ-$LiAlO_2$ pallet irradiated at 773 K to 2×10^{17} $(He^+ + D^+)/cm^2$ at a medium dose rate of 2.9×10^{-4} dpa/s, acquired at (a) and (b) medium and (c) high magnifications.

The corresponding microstructure of the irradiated region is presented in Fig. 12. Similar to the high dose-rate specimen, the region exhibits a three-layered morphology consisting of (i) an amorphous surface layer, (ii) an interface enriched with cavities, and (iii) an underlying crystalline matrix containing nanoscale $LiAl_5O_8$ precipitates. The amorphous surface layer in this medium dose-rate sample measures ~170 nm on the [001] orientation projection, considerably thinned than the ~285 nm observed on the [100] projection in the high dose-rate case [Fig. 10(b)]. The origin of this difference in amorphous layer thickness remains uncertain, but two factors may contribute: (1) the reduced electronic energy deposition rate at the lower dose rate could decrease the probability of amorphization for a given electronic stopping power, and (2) crystallographic anisotropy may result in direction-dependent in disordering behavior of γ-$LiAlO_2$. Unlike the high dose-rate specimen, the cavity-enriched interface in this sample does not show a well-developed blister morphology (such as that observed in Fig. 10). However, the absence of a blister in the imaged region does not necessarily rule out its formation elsewhere, as blistering is typically heterogeneous and may depend on local grain orientation and gas accumulation sites.

Atomic-level resolution STEM imaging of an individual $LiAl_5O_8$ precipitate embedded within the crystalline region reveals a well-defined twin boundary, as shown by the yellow dashed line in the inset of Fig. 12(c). In the projection plane, the boundary is oriented parallel to the γ-$LiAlO_2$ [200] (equivalently [100]) crystallographic direction, as determined from the diffraction pattern in Fig. 12(a). Based on the previously established orientation relationship between the cubic $LiAl_5O_8$ precipitates and the tetragonal γ-$LiAlO_2$ matrix, i.e., $LiAl_5O_8$ [111] // γ-$LiAlO_2$ [100],[5,9] the observed boundary plane within the $LiAl_5O_8$ precipitate is identified as belonging to the $LiAl_5O_8$ {111} family. This crystallographic alignment provides a clear basis for the anisotropic morphology of the precipitates observed in projection.

To further investigate the microstructural characteristics from a different crystallographic perspective, the same grain was tilted toward the γ-$LiAlO_2$ [101] zone axis, as shown in the inset of Fig. 13(a). STEM imaging under this orientation reveals microstructural features consistent with those observed along the [100] zone axis, including the presence of an amorphous surface layer, a cavity-rich interfacial region, and an underlying crystalline region containing $LiAl_5O_8$ precipitates.

c. Low dose-rate case

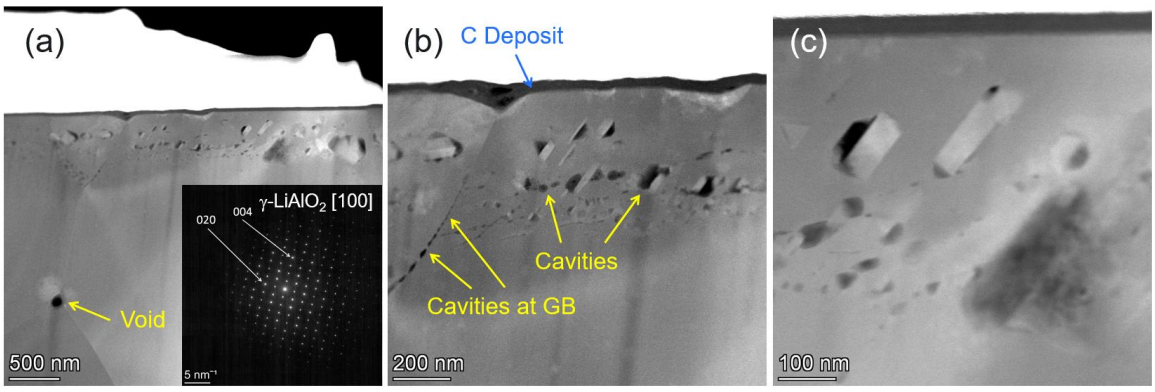

FIG. 14. STEM micrographs showing the microstructure of a [100]-oriented γ-$LiAlO_2$ pallet irradiated to 2×10^{17} $(He^+ + D^+)/cm^2$ at 773 K with a low dose rate of 6.8×10^{-5} dpa/s, acquired at (a) low, (b) medium, and (c) high magnifications.

The inset in Fig. 14(a) presents the experimental SAED pattern acquired from a crystalline γ-$LiAlO_2$ grain in the FIB-prepared specimen irradiated to a combined fluence of 2×10^{17} $(He^+ + D^+)/cm^2$ at 773 K under a low dose rate of 6.8×10^{-5} dpa/s. The data confirms that the grain is aligned along the [100] axis. Fig. 14 illustrates the microstructural features of the irradiated region at multiple magnifications. In striking contrast to the microstructures observed at medium and high dose rates, no continuous amorphous layer is detected across the irradiated depth. Instead, the region remains fully crystalline, suggesting that at this low dose rate, the defect production and simultaneous defect recovery are well balanced. Within the crystalline γ-$LiAlO_2$ matrix, numerous $LiAl_5O_8$ precipitates are observed, accompanied with cavities along grain boundaries, around precipitates, and within the bulk matrix, indicating that vacancy–gas clustering and cavity nucleation occur across a range of microstructural sites rather than being localized at a specific depth. The co-existence of cavities and precipitates within the same crystalline volume suggests that local gas retention and phase separation processes are active at the low dose rate.

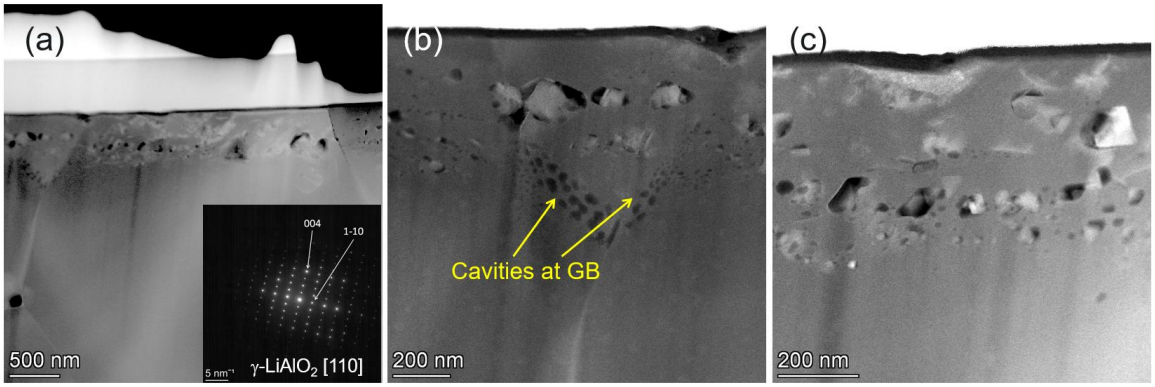

FIG. 15. STEM micrographs showing the microstructure of a [110]-oriented γ-$LiAlO_2$ pallet irradiated to 2×10^{17} $(He^+ + D^+)/cm^2$ at 773 K with a low dose rate of 6.8×10^{-5} dpa/s, acquired at (a) low, (b) and (c) medium magnifications.

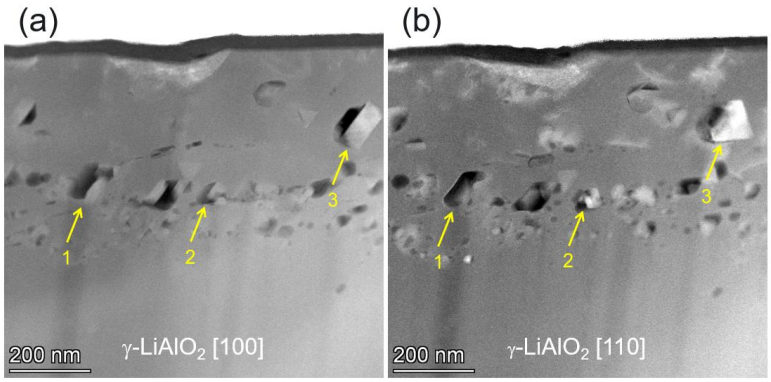

FIG. 16. Comparison of the microstructures in the γ-$LiAlO_2$ pellet sample irradiated to 2×10^{17} $(He^+ + D^+)/cm^2$ at 773 K with a low dose rate of 6.8×10^{-5} dpa/s, observed along the (a) [100] and (b) [110] crystallographic axes.

To examine the orientation dependence of these features, the same grain was tilted by 45°, aligning it along the [110] zone axis, as confirmed by the diffraction pattern shown in the inset of Fig. 15(a). The microstructure exhibits similar morphological characteristics to those seen along [100]. Aggregated cavities are prominently distributed along grain boundary planes, and their clear visibility in the off-edge viewing direction provides compelling evidence that cavity nucleation and growth preferentially occur along grain boundaries, where defect sinks facilitate vacancy and gas accumulation.

To better understand the three-dimensional morphology of precipitates and cavities, Fig. 16 compares microstructural images acquired along both [100] and [110] orientations for the same irradiated grain. Arrows labeled 1–3 mark selected precipitates visible in both projections. Upon rotating the grain by 45°, each precipitate exhibits a noticeable change in its apparent shape and projected dimensions. For example, precipitate 3 appears rectangular when viewed along [100] but transforms into a triangular morphology along [110]. These shape variations underscore the anisotropic geometry and faceting of the precipitates. Such multi-orientation observations are essential for better microstructural interpretation, as single-view imaging may underestimate the true morphological complexity of irradiation-induced features. The

consistent crystallinity, lack of amorphization, and extensive cavity decoration along grain boundaries together indicate that low-dose-rate irradiation at 773 K promotes defect recovery, suppresses amorphization, and favors vacancy/gas redistribution along structural sinks. This behavior contrasts sharply with the amorphous layer formation and blistering observed under higher dose-rate conditions, suggesting that dose rate exerts a critical influence on the competition between defect accumulation, new phase precipitation, and blister evolution during irradiation of γ-$LiAlO_2$.

It should be noted that no cavities were detected within the nanoscale $LiAl_5O_8$ precipitates. One possible explanation is that the small size of the precipitates and the associated interfacial constraints with the surrounding γ-$LiAlO_2$ matrix may inhibit stable cavity nucleation and growth. In nanoscale regions, the energetics of vacancy clustering and gas stabilization can differ substantially from those in larger crystalline volumes, and the high interfacial area may suppress the formation or growth of stable cavities. In contrast, irradiation-induced planar defects in micron-sized grains have recently been reported[21] to evolve into likely gas-filled elongated cavities under irradiation conditions, suggesting that such defect evolution may be more favorable in larger volumes than within nanoscale precipitates.

d. Comparison of microstructure and precipitate size

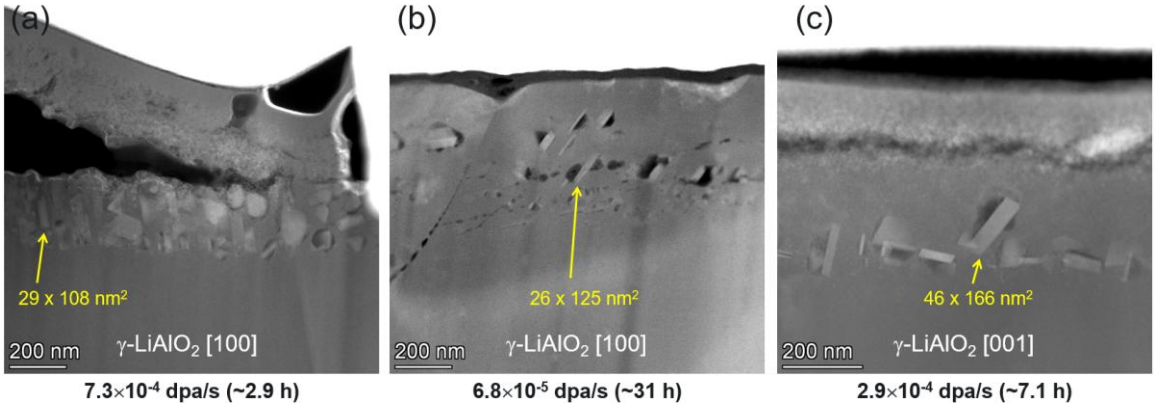

FIG. 17. STEM micrographs showing the microstructures of [100]- and [001]-oriented γ-$LiAlO_2$ pallets irradiated to 2×10^{17} $(He^+ + D^+)/cm^2$ at 773 K, with dose rates of (a) 7.3×10^{-4}, (b) 6.8×10^{-5}, and (c) 2.9×10^{-4}.

Fig. 17 compares the microstructures of γ-$LiAlO_2$ grains irradiated to a combined fluence of 2×10^{17} $(He^+ + D^+)/cm^2$ at 773 K under three different dose rates, with imaging conducted along both the [100] and [001] zone axes. The ordering of the images in Fig. 17 is arranged so that the low- and high-dose-rate conditions are placed adjacent to each other, as they were imaged along the same crystallographic orientation [100] and therefore allow a direct comparison. The medium-dose-rate image was obtained along a different orientation [001] and is included primarily to illustrate the orientation dependence of the apparent precipitate dimensions. Because of this difference in viewing direction, a direct quantitative comparison between the medium-dose-rate condition and the other two cases is limited.

Quantitative analysis of precipitate dimensions shows typical projected sizes of 29 nm × 108 nm for the high-dose-rate sample and 26 nm × 125 nm for the low-dose-rate sample [Figs. 17(a) and 17(b)]. To facilitate comparison of precipitate dimensions viewed along different directions under different

Table III. Representative dimensions of $LiAl_5O_8$ precipitates in γ-$LiAlO_2$ irradiated to 2×10^{17} $(He^+ + D^+)/cm^2$ at 773 K under different dose rates and observation directions.

Matrix Orientation	High Dose Rate (7.3×10^{-4} dpa/s)	Low Dose Rate (6.8×10^{-5} dpa/s)	Medium Dose Rate (2.9×10^{-4} dpa/s)
γ-$LiAlO_2$ [100]	29 × 108 nm^2	26 × 125 nm^2	---
γ-$LiAlO_2$ [001]	---	---	46 × 166 nm^2
γ-$LiAlO_2$ [110]	24 × 71 nm^2	19 × 96 nm^2	---
γ-$LiAlO_2$ [101]	---	---	28 × 128 nm^2

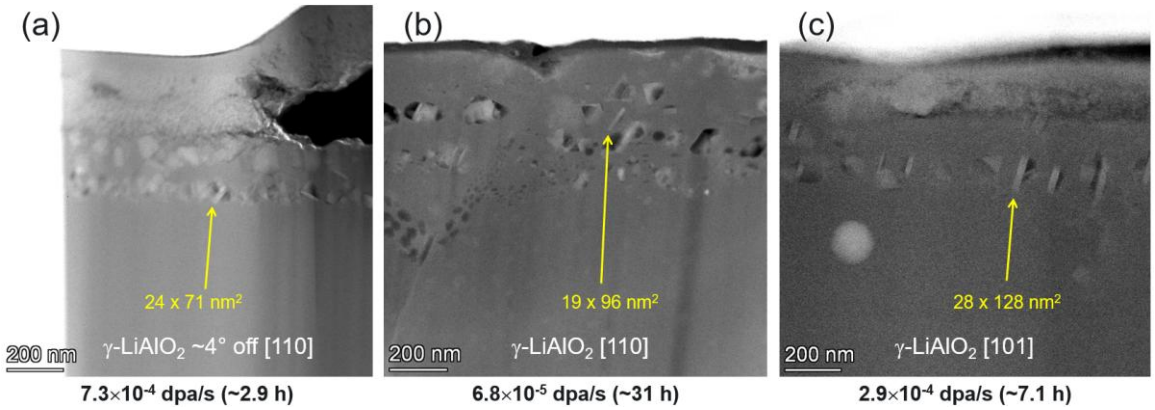

FIG. 18. STEM micrographs showing the microstructures of [110]- and [101]-oriented γ-$LiAlO_2$ pallets irradiated to 2×10^{17} $(He^+ + D^+)/cm^2$ at 773 K, with dose rates of (a) 7.3×10^{-4}, (b) 6.8×10^{-5}, and (c) 2.9×10^{-4}.

irradiation conditions, the measured sizes of precipitates in γ-$LiAlO_2$ are summarized in Table III. These results indicate that, within this dose-rate range (6.8×10^{-5} to 7.3×10^{-4} dpa/s), the overall influence of dose rate on precipitate size is relatively modest. However, the similarity in precipitate size across this range should not be interpreted as evidence that size is independent of dose rate. In prior neutron irradiation experiments performed under thermalized fission neutron spectra at 573 K, where dose rates were two to three orders of magnitude lower, the resulting $LiAl_5O_8$ precipitates reached micron-scale dimensions. This comparison suggests that precipitate coarsening does not scale linearly with dose rate, and that slower irradiation conditions promote greater diffusion-mediated growth over longer timescales.

In the medium-dose-rate sample, the observed precipitates appear slightly larger, with an average projected size of 46 nm × 166 nm [Fig. 17(c)]. This apparent size difference likely arises from anisotropic growth kinetics associated with the tetragonal crystal structure of γ-$LiAlO_2$, where precipitate growth can proceed at different rates along distinct crystallographic directions. Such anisotropy is consistent with the established orientation relationships between the $LiAl_5O_8$ precipitates and γ-$LiAlO_2$ matrix, which favor faceted growth along specific low-index planes.

Beyond precipitate morphology, dose rate also influences the distribution and behavior of implanted gas species. At the low dose rate, helium and deuterium accumulation appears more spatially dispersed, forming isolated, likely gas-filled cavities at multiple structural sites, including within the matrix, around precipitates, and along grain boundaries. This dispersed distribution suggests that at lower dose rates, defect annihilation and gas release processes have sufficient time to occur, preventing the buildup of high local gas pressures. In contrast, at the high dose rate, implanted gas atoms exhibit a stronger tendency to migrate and accumulate at the crystalline-amorphous interface, producing large blisters and aggregated cavities. The localization of gas accumulation at this interface indicates a strong coupling between damage accumulation, gas trapping, and amorphization kinetics, where rapid defect generation outpaces defect recovery. This behavior implies that higher dose rates enhance the effective mobility of implanted gases by increasing the transient defect concentration and promoting gas transport along defect-rich paths.

A further comparison of microstructures imaged along or near the [110] axis is provided in Figs. 18(a) and 18(b). The same general trends are observed: the high- and low-dose-rate samples exhibit comparable precipitate sizes, while the medium-dose-rate sample again displays slightly larger precipitates when examined along [101]. These consistent observations across multiple viewing directions reinforce that the apparent precipitate size difference primarily reflects crystallographic anisotropy rather than an intrinsic dependence on dose rate within the studied range. Overall, the results in Figs. 17 and 18 demonstrate that while precipitate size remains relatively insensitive to dose rate between 6.8×10^{-5} and 7.3×10^{-4} dpa/s, gas behavior and amorphization response are markedly dose-rate dependent. High dose rates promote localized gas accumulation and amorphous layer formation, whereas low dose rates favor crystallinity retention, cavity dispersion, and defect recovery.

3. Deuterium retention and lithium depletion

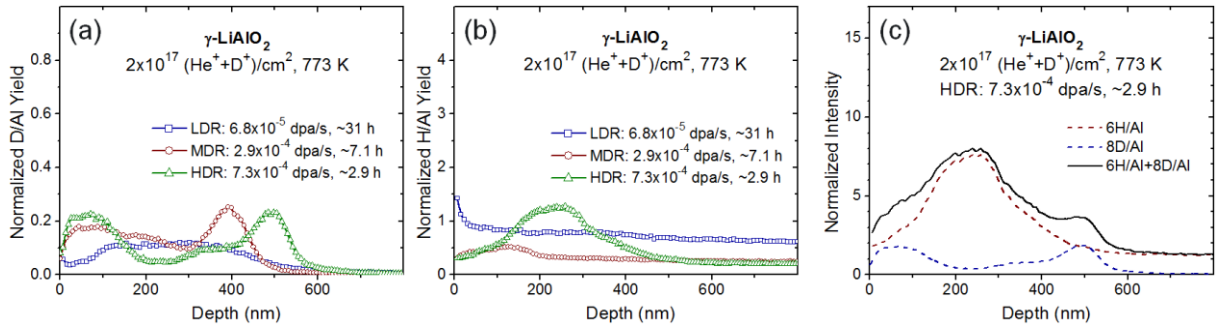

FIG. 19. ToF-SIMS depth profiles of normalized (a) D/Al and (b) H/Al yields in γ-$LiAlO_2$ pellets irradiated to 2×10^{17} $(He^+ + D^+)/cm^2$ at 773 K, with dose rates of 6.8×10^{-5}, 2.9×10^{-4} and 7.3×10^{-4} dpa/s. (c) Relative concentrations of H, D, and their sum in the pellet irradiated at 7.3×10^{-4} dpa/s.

Figures 19(a) and (b) presents the normalized ToF-SIMS depth profiles of D and H, shown relative to Al yields, in γ-$LiAlO_2$ pellets irradiated to a combined fluence of 2×10^{17} $(He^+ + D^+)/cm^2$ at 773 K under three different dose rates. At the high dose rate of 7.3×10^{-4} dpa/s, the D depth profile exhibits a distinct double-peak structure [Fig. 19(a)], accompanied by a corresponding H peak at the same depth [Fig. 19(b)]. This correlated behavior is again attributed to isotopic exchange between H and D, as discussed above. The relative concentrations of H, D, and their sum shown in Fig. 19(c) for the high-dose-rate case

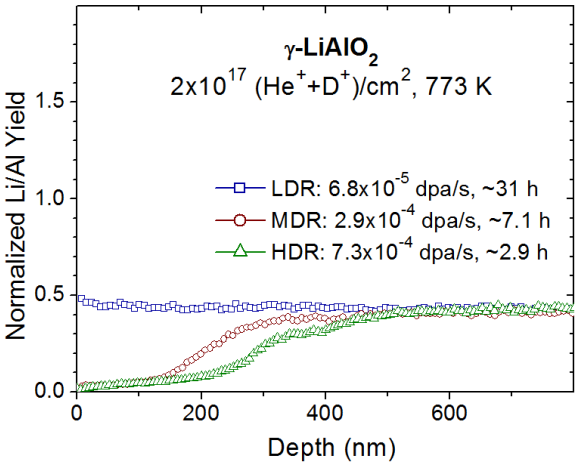

FIG. 20. ToF-SIMS depth profiles of normalized Li/Al yields in γ-$LiAlO_2$ pellets irradiated to 2×10^{17} $(He^+ + D^+)/cm^2$ at 773 K, with dose rates of 6.8×10^{-5}, 2.9×10^{-4} and 7.3×10^{-4} dpa/s.

were estimated using the same methodology described for Fig. 7(c). Both figures exhibit consistent trends, with the protium concentration dominating within the irradiated region.

The influence of dose rates on isotopic exchange is evident when comparing different irradiation conditions. At the high dose rate, the rapid buildup of D concentration creates a localized peak where isotopic exchange is most likely to occur, leading to the observed double-peak structure. In contrast, at lower dose rates, isotopic exchange is minimal throughout the irradiated depth. This behavior likely arises from the slower accumulation of D concentration, which reduces the probability of trapped D being exchanged with migrating H from the environment at 773 K. It should be noted that minor isotopic exchange of H-D may still occur even when a distinct D dip cannot be resolved.

Figure 20 shows the normalized Li/Al yields as a function of depth for the same samples. At the high dose rate of 7.3×10^{-4} dpa/s, significant Li depletion is observed during irradiation, extending from the surface to a depth of ~300 nm, mainly within the amorphized surface region [Fig. 11(b)]. At the medium dose rate of 2.9×10^{-4} dpa/s, Li depletion is less pronounced and largely confined to the amorphized surface layer [Fig. 12(b)]. These results are consistent with earlier observations of Li loss in γ-$LiAlO_2$ pellets irradiated at 773 K.[5,7] In contrast, the low dose-rate sample (6.8×10^{-5} dpa/s) exhibits no measurable Li depletion and no surface amorphization. It should be noted that minor Li loss may still occur under the irradiation conditions, but distinguishing it from the much higher initial Li concentration is beyond the resolution of this study.

The observed Li depletion under high dose rate irradiation indicates a dose-rate-dependent kinetic process governed by the balance between defect production and dynamic recovery. Under low dose rate irradiation, the rate of defect generation is relatively low, allowing efficient recombination of irradiation-induced point defects, including Li interstitials. At the elevated irradiation temperature used in this study, these defects are sufficiently mobile to annihilate before accumulating to concentrations required for large-scale structural disorder or amorphization. Consequently, the density of irradiation-induced defects that could facilitate long-range Li migration remains limited, and no measurable net Li loss is detected in γ-$LiAlO_2$. In contrast, under high dose rate irradiation the defect production rate exceeds the recombination rate, leading to enhanced accumulation of point defects and defect clusters. The resulting

increase in structural disorder can significantly enhance Li mobility by providing faster diffusion pathways. In the near-surface region, electronic excitation and ionization associated with ion irradiation may further enhance Li out-diffusion. These combined effects increase the driving force for Li migration toward the surface, where Li can be removed through evaporation or sputtering. As a result, significant Li depletion and phase amorphization can occur in the near-surface region of γ-$LiAlO_2$. Previous atom probe tomography (APT) measurements[6] have shown that the concentrations of Li, Al, and O in the amorphized layer vary with depth and location, reflecting significant compositional redistribution during irradiation. Under conditions of severe Li depletion, the residual composition would be expected to approach that of Al_2O_3.

C. Discussion of Methodology, Ion vs. Neutron Radiation Damage, and Mechanisms

1. Physical basis and limitations of sequential ion irradiation methodology

Ion irradiation is widely used to investigate radiation effects in various nuclear materials, including tritium-breeding lithium ceramics; however, it should be recognized that no ion-irradiation approach can fully reproduce neutron irradiation conditions. In particular, ion irradiation cannot simultaneously replicate the complete primary knock-on atom (PKA) energy spectrum, neutron-induced transmutation reactions, or the exact spatial and temporal coupling between displacement damage and gas production. The objective of the sequential irradiation approach used in this study is therefore not to establish quantitative equivalence with neutron irradiation, but rather to reproduce the dominant defect structures and their interactions with hydrogen isotopes under controlled conditions. The sequential He^+ and D_2^+ irradiations employed in our previous studies reproduce the same characteristic microstructural features and H isotope behavior in neutron-irradiated γ-$LiAlO_2$. Dual-beam (simultaneous) He^+ and D_2^+ irradiation experiments are, in principle, more representative of neutron irradiation conditions because they more closely mimic the concurrent production of displacement damage and transmutation gases. However, preliminary results from our dual-beam irradiation experiments on γ-$LiAlO_2$ pellets indicate microstructural evolution similar to that observed under sequential irradiation. This similarity may suggest that the dominant defect interactions and precipitation processes are primarily governed by displacement damage and helium-stabilized defect structures, rather than by the exact temporal sequence of gas implantation. The dual-beam data are currently under analysis and will be reported in a forthcoming publication.

The irradiation sequence used in this study consisted of He^+ irradiation followed by D_2^+ implantation. This sequence was selected because helium is known to strongly influence vacancy clustering and cavity nucleation in many irradiated materials. Introducing He prior to D implantation promotes the formation of He-stabilized vacancy clusters that can serve as trapping sites for subsequently implanted D in γ-$LiAlO_2$. In addition, under the present irradiation conditions most of the displacement damage is generated by the heavier He^+ ions. Performing He^+ irradiation first therefore establishes the primary population of radiation-induced defects (vacancies, interstitial clusters, and early-stage cavities), while the subsequent D_2^+ implantation primarily probes the interaction of deuterium with these pre-existing defects rather than significantly redefining the damage structure. A previous ion irradiation study[9] of single crystal γ-$LiAlO_2$ has shown a higher dechanneling yields in Rutherford backscattering spectrometry under channeling conditions (RBS/C) for irradiation sequence $H_2^+ \rightarrow He^+$, suggesting a greater degree of lattice distortion associated with differences in the resulting cavity population. However, a detailed microstructural

comparison between the two irradiation sequences has not yet been performed. A systematic investigation of microstructural evolution under different irradiation orders will be the subject of future work.

Pramanik and Seidman[22] have shown that low-energy heavy dimers (40 keV W_2^+ and Ag_2^+) in a regime dominated by nuclear stopping can enhance cascade overlap near the surface, significantly increasing surface damage and sputtering. The use of molecular D_2^+ ions for irradiation in this study is likewise expected to enhance the surface sputtering to some extent; however, the overall sputtering yield remains low because of the light mass of deuterium. Energetic molecular ions dissociate rapidly upon entering a solid because the molecular binding energy is small compared with the kinetic energy of the incident ion. As discussed in ion–solid interaction studies,[23,24] the constituent atoms typically separate after traveling only a few Å in the target. After this very short distance, the ions propagate independently and behave as separate atomic ions. For the 80 keV D_2^+ irradiation used in this study of γ-$LiAlO_2$, the molecular ion dissociates within the first few atomic layers near the surface, after which two 40 keV D^+ ions propagate independently through the lattice. Because the projected ion range in γ-$LiAlO_2$ is on the order of hundreds of nanometers, molecular correlation effects are confined to a very thin surface region (<1 nm) and do not significantly influence the damage evolution or deuterium transport behavior in the bulk of the irradiated region considered in this work.

During ion irradiation, a magnetic rastering system was employed to ensure lateral dose uniformity across the intended irradiation area (~5 mm × 10 mm). Prior to rastering, the ion beam was not tightly focused and had an average spot size of approximately 2 mm × 4 mm. The magnetic scanning frequencies were relatively low (2.9 Hz horizontally and 0.31 Hz vertically), so the rastering primarily serves to spatially average the ion flux across the target area rather than introduce pulsed irradiation conditions.

During ion irradiation, the sample temperature was continuously monitored using a thermocouple attached to the copper sample holder and actively controlled within ±5 K of the set point. The temperature difference between the holder and the sample surface was measured to be within 10 K over the temperature range investigated in this study. To evaluate potential beam-heating effects, the measured temperature was compared under beam-on and beam-off conditions at the highest dose rate used. The observed temperature difference was within ~5 K, indicating that beam-induced heating was minimal. Several experimental factors contributed to this limited heating results, including the excellent thermal conductivity of the sample holder, relatively low ion energies, and the magnetic rastering over a large irradiation area, which reduced the local power density at the surface of the γ-$LiAlO_2$ samples. Under these conditions, steady-state heat dissipation through the sample holder is efficient, and no measurable temperature excursions beyond the ±5 K control range were detected. This variation is small compared with the overall temperature range investigated in this study (623–773 K) and is therefore not expected to significantly influence defect mobility, cavity formation, amorphization behavior, or precipitation trends.

2. Comparison of γ-$LiAlO_2$ pellets irradiated with ions and neutrons

Fig. 21(a) shows the microstructure of a γ-$LiAlO_2$ pellet irradiated to 2×10^{17} $(He^+ + D^+)/cm^2$ at 773 K with a low dose rate of 6.8×10^{-5} dpa/s. As indicated in the figure, several characteristic irradiation-induced features are observed. Faceted precipitates form within the grain interiors, accompanied by cavities both surrounding the precipitates and distributed in the γ-$LiAlO_2$ matrix. Cavities also exhibit a tendency to aggregate along grain boundaries. In addition, well-defined denuded zones are present adjacent to grain boundaries and near the surface, where the density of precipitates vanishes. These

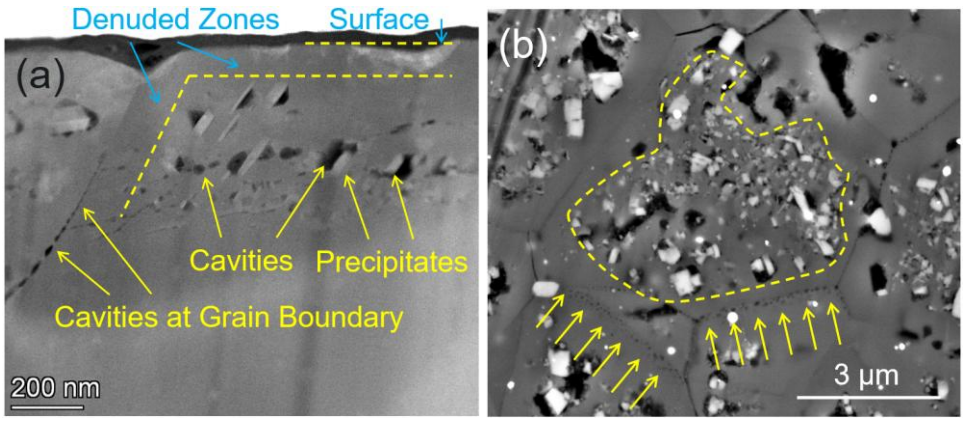

FIG. 21. Comparison of microstructures in γ-$LiAlO_2$ pellets irradiated with (a) He^+ and D_2^+ ions at 773 K and (b) thermalized fission neutron spectrum at 573 K.

features collectively indicate active defect migration and preferential defect annihilation at extended sinks such as grain boundaries and surfaces during irradiation at elevated temperature.

For comparison, Fig. 21(b) shows the microstructure of the same type of γ-$LiAlO_2$ pellet irradiated with thermalized fission neutrons at 573 K, producing a comparable helium concentration but at a dose rate approximately 400 times lower than that used in the ion irradiation experiment. Despite differences in irradiation temperature and dose rate, the overall microstructural characteristics are remarkably similar. The neutron-irradiated specimen also exhibits faceted precipitates that preferentially form within the central regions of grains, separated from grain boundaries by clearly defined denuded zones. Cavities are observed both within the γ-$LiAlO_2$ matrix and in association with the precipitates. In addition, several grain boundaries show pronounced cavity accumulation, as indicated by the arrows in Fig. 21(b). The principal difference between the two cases is the characteristic size scale of the irradiation-induced features, which is approximately an order of magnitude larger in the neutron-irradiated γ-$LiAlO_2$, consistent with the significantly lower dose rate and longer time available for defect migration and coarsening.

Additional observations reported in the literature further support the similarity between ion- and neutron-irradiation responses in γ-$LiAlO_2$. Lithium depletion from γ-$LiAlO_2$ pellets during irradiation has been reported under both neutron and ion irradiation conditions,[7,8] suggesting that comparable radiation-induced compositional evolution processes occur in the two environments. Moreover, previous studies[2] comparing hydrogen isotope release behavior have shown that deuterium release measured during ion irradiation is quantitatively consistent with tritium release from neutron-irradiated γ-$LiAlO_2$ pellets when comparable gas inventories are considered. Isotopic exchange behavior observed in the present ion irradiation study has also been reported in neutron-irradiated materials.[18]

Although ion irradiation cannot reproduce all aspects of neutron irradiation, most notably nuclear transmutation reactions and the associated long-term compositional changes, the dominant defect processes governing microstructural evolution follow the same underlying physical mechanisms. These processes include irradiation-induced vacancy and interstitial production, defect clustering, helium-stabilized cavity nucleation, cavity growth and coalescence, defect absorption at sinks leading to grain-boundary and surface denudation, and hydrogen isotope trapping and release. The strong correspondence

in both microstructural features and gas-behavior observations therefore provides further support for the use of ion irradiation as a valuable experimental approach for investigating radiation-induced defect evolution and gas behavior in γ-$LiAlO_2$.

From a practical standpoint, an irradiation temperature of ~773 K is recommended for sequential He^+ and D^+ ion irradiation at low dose rates on the order of ~5×10^{-5} dpa/s to replicate the microstructural characteristics of γ-$LiAlO_2$ irradiated in a thermalized fission neutron spectrum at 573 K. To compensate for enhanced gas release at elevated ion irradiation temperatures, a higher total ion fluence should be applied to maintain comparable implanted gas concentrations while promoting the growth of larger $LiAl_5O_8$ precipitates, more closely resembling those observed in neutron-irradiated γ-$LiAlO_2$ at 573 K.[2]

3. Mechanism discussion

Under energetic ion irradiation, defect generation in γ-$LiAlO_2$ arises from both electronic and nuclear processes. Electronic energy deposition can ionize lattice atoms and break chemical bonds, leading to local decomposition, or excite atoms and enhance their mobility. In parallel, nuclear stopping produces displacement cascades through atomic collisions, generating vacancies, interstitials, and possibly small defect clusters. The resulting steady-state defect population is governed by the kinetic competition between defect production and dynamic recovery processes, including recombination, migration, and thermally activated annihilation. This balance depends strongly on temperature and dose rate. At lower dose rates, the time between successive displacement events allows efficient recombination and migration of point defects, resulting in relatively low steady-state defect concentrations. At higher dose rates, defect production can outpace recovery processes, leading to elevated concentrations of vacancies, interstitials, and defect clusters. These non-equilibrium defect populations can significantly enhance radiation-induced transport processes. At a given dose rate, increasing temperature accelerates point-defect migration and promotes both recombination and clustering.

Under high dose-rate irradiation at elevated temperature, electronic excitation contributes to surface amorphization and Li depletion in the near-surface region through radiation-induced decomposition and enhanced Li diffusion in γ-$LiAlO_2$. Li depletion modifies the local bonding environment and reduces the stability of the crystalline lattice, facilitating the persistence of the amorphous surface layer. In contrast, the damage-peak region retains crystallinity due to efficient dynamic defect recovery, and $LiAl_5O_8$ precipitates and cavities form as a result of Li migration and redistribution. Under lower dose-rate conditions, which more closely resemble neutron irradiation, complete surface amorphization does not occur and Li loss is not measurable in the present study.

These mechanisms provide a consistent framework linking irradiation-induced defect generation, defect kinetics, radiation-enhanced Li diffusion, and the phase transformations observed in this study.

IV. CONCLUSIONS

This study systematically investigated the effects of irradiation temperature and dose rate on microstructural evolution, hydrogen isotope behavior, and lithium redistribution in γ-$LiAlO_2$ subjected to sequential He^+ and D_2^+ ion irradiation. The results provide new insights into the kinetic competition between radiation-induced defect production and thermally activated defect recovery, and they help

establish conditions under which ion irradiation can effectively emulate neutron irradiation environments relevant to tritium-breeding ceramics.

First, irradiation temperature strongly governs the transition in radiation damage mechanisms. At 623 K, irradiation produces cavities and fractures near the helium damage peak but does not induce second-phase precipitation, indicating limited atomic mobility and suppressed phase transformation. When the temperature increases to 673 K, small precipitates begin to nucleate together with cavities and fractures, marking the onset of irradiation-enhanced chemical segregation. Further increasing the temperature to 723–773 K results in significant precipitate coarsening and the formation of large, faceted $LiAl_5O_8$ precipitates near the damage peak, accompanied by cavity networks and a persistent amorphous surface layer. These observations demonstrate a clear temperature-dependent transition from a cavity-dominated microstructure at lower temperatures to a precipitate-dominated microstructure at higher temperatures.

Second, irradiation temperature strongly influences hydrogen isotope redistribution. At temperatures ≤723 K, hydrogen trapping is primarily associated with irradiation-induced defects in the He damage region, and isotopic exchange between H and D remains limited. At 773 K, however, enhanced atomic mobility activates isotopic exchange processes, leading to the formation of characteristic double-peak structures in the D depth profiles and corresponding H enrichment. These results indicate that isotopic exchange becomes an important mechanism governing hydrogen isotope redistribution and potential tritium release behavior at elevated temperatures.

Third, lithium redistribution and depletion are closely linked to radiation-induced structural disorder. Significant Li depletion is observed only at 773 K and is primarily confined to the amorphized near-surface region. This Li loss is attributed to irradiation-enhanced Li diffusion toward the surface combined with volatilization and sputtering processes. At lower irradiation temperatures (≤723 K), Li mobility remains limited and no measurable Li depletion is detected within the experimental resolution.

Dose rate also plays a critical role in determining the radiation response of γ-$LiAlO_2$ at 773 K. Under high dose-rate conditions, intense radiolysis promotes amorphization in the near-surface region, leading to the formation of a distinct amorphous layer, significant Li depletion, localized gas accumulation, and surface blistering. In contrast, low dose-rate irradiation allows efficient dynamic defect recovery, preserving the crystalline structure throughout the irradiated region. Under these conditions, $LiAl_5O_8$ precipitates and cavities form within the crystalline matrix, with cavities preferentially accumulating along grain boundaries and around precipitates. These observations highlight the strong kinetic control exerted by dose rate on the balance between defect accumulation, amorphization, and gas redistribution.

Despite substantial differences in irradiation conditions, the microstructural features observed in ion-irradiated γ-$LiAlO_2$, such as $LiAl_5O_8$ precipitate formation, cavity development, grain-boundary cavity aggregation, and denuded zones, closely resemble those in neutron-irradiated material. The primary distinction lies in the characteristic size scale of these features, which is larger under neutron irradiation due to the orders-of-magnitude lower dose rates and longer defect evolution times. This correspondence demonstrates that the sequential He^+ and D^+ ion irradiation approach can successfully reproduce the dominant radiation damage mechanisms in γ-$LiAlO_2$.

Overall, the results establish that ion irradiation at ~773 K with low dose rates on the order of ~5×10^{-5} dpa/s can effectively emulate the microstructural evolution observed in γ-$LiAlO_2$ irradiated in a thermalized neutron spectrum at ~573 K. These findings provide a mechanistic framework linking defect

production, defect kinetics, gas trapping, isotopic exchange, and lithium transport under irradiation. The study also offers practical guidance for designing ion irradiation experiments that more closely reproduce reactor-relevant conditions, thereby improving the predictive understanding of radiation effects and tritium behavior in lithium-based tritium breeder ceramics.

CRediT authorship contribution statement

Weilin Jiang: Writing - original draft, Supervision, Project administration, Funding acquisition, Methodology, Investigation, Formal analysis, Data curation, Conceptualization. **Libor Kovarik:** Methodology, Investigation, Formal analysis. **Zihua Zhu:** Methodology, Investigation. **Karen Kruska:** Investigation. **Xin Zhang:** Investigation. **Xiaoxu Li:** Investigation. **Zhihan Hu:** Investigation. **Lin Shao:** Supervision, Resources. **Andrew Casella:** Writing – review & editing, Program administration, Resources. **David Senor:** Writing – review & editing, Program administration, Resources.

Declaration of competing interest

The authors have no conflicts to disclose.

Data availability

The data that support the findings of this study are available from the corresponding author upon reasonable request.

ACKNOWLEDGEMENTS

This research was supported by Tritium Modernization Program, sponsored by National Nuclear Security Administration of the U.S. Department of Energy, and performed at the Pacific Northwest National Laboratory under contract DE-AC05-76RL01830. The image shown in Fig. 21 (b) is courtesy of D. J. Edwards at PNNL. The authors gratefully acknowledge Alec C. Pfundheller and Benjamin E.M. Diaz (Texas A&M University) for assistance with ion irradiation experiments. ToF-SIMS analyses were performed at the Environmental Molecular Sciences Laboratory within PNNL.

REFERENCES

[1]W. Jiang, A. Roy, X. Zhang, L. Kovarik, Z. Zhu, X. Li, M. H. Weber, J. S. McCloy, Z. Hu, L. Shao, A. M. Casella, and D. J. Senor, Volumetric swelling in $LiAl_5O_8$ and γ-$LiAlO_2$ pellets under ion irradiation, to be published, 2026.
[2]W. Jiang, W. G. Luscher, T. Wang, Z. Zhu, L. Shao, and D. J. Senor, J. Nucl. Mater. **542,** 152532 (2020).
[3]W. Jiang, S. R. Spurgeon, Z. Zhu, X. Yu, K. Kruska, T. Wang, J. Gigax, L. Shao, and D. J. Senor, J. Nucl. Mater. **511,** 1 (2018).
[4]W. Jiang, T. Wang, Y. Wang, Z. Zhu, L. Shao, and D. J. Senor, J. Nucl. Mater. **538,** 152357 (2020).
[5]W. Jiang, L. Kovarik, Z. Zhu, T. Varga, M. E. Bowden, B. E. Matthews, Z. Hu, L. Shao, and D. J. Senor, J. Appl. Phys. **131,** 215902 (2022).

[6]W. Jiang, L. Kovarik, M. G. Wirth, Z. Hu, L. Shao, A. M. Casella, and D. J. Senor, J. Nucl. Mater. **591,** 154925 (2024).
[7]W. Jiang, J. Zhang, D. J. Edwards, N. R. Overman, Z. Zhu, L. Price, J. Gigax, E. Castanon, L. Shao, and D. J. Senor, J. Nucl. Mater. **494,** 411 (2017).
[8]X.-Y. Yu, J. Yao, B. Matthews, S. R. Spurgeon, S. Riechers, G. Sevigny, Z. Zhu, W. Jiang, and W. G. Luscher, J. Mater. Res. Technol. **14,** 475 (2021).
[9]W. Jiang, J. Zhang, L. Kovarik, Z. Zhu, L. Price, J. Gigax, E. Castanon, X. Wang, L. Shao, and D. J. Senor, J. Nucl. Mater. **484,** 374 (2017).
[10]S. L. Dudarev, M. R. Gilbert, K. Arakawa, H. Mori, Z. Yao, and M. L. Jenkins, J. Nucl. Mater. **455,** 16 (2014).
[11]W. Jiang, Y. Zhu, L. Zhang, D. J. Edwards, N. R. Overman, G. Nandipati, W. Setyawan, C. H. Henager Jr., and R. J. Kurtz, J. Nucl. Mater. **550,** 152905 (2021).
[12]L. N. Clowers, Z. Jiao, and G. S. Was, J. Nucl. Mater. **565,** 153722 (2022).
[13]J. F. Ziegler, J. P. Biearsack, and U. Littmark, The stopping and Range of Ions in Solids (Pergamon Press, New York, 1985); available at: http://www.SRIM.org/.
[14]H. Tsuchihira, T. Oda, and S. Tanaka, Nucl. Instr. Meth. Phys. Res. B **269,** 1707 (2011).
[15]S. Agarwal, Y. Lin, C. Li, R. E. Stoller, and S. J. Zinkle, Nucl. Inst. Meth. Phys. Res. B. **503,** 11 (2021).
[16]Y.-R. Lin, S. J. Zinkle, C. J . Ortiz, J.-P. Crocombette, R. Webb, and R. E. Stoller, Curr. Opin. Solid State Mater. Sci. **27,** 101120 (2023).
[17]Y. Zhou, J.A. Dhas, M. Xia, V. Suseela, H.-M. Kao, R.M. Asmussen, A. Bhattacharjee, C.A. Creamer, M. Liu, J.-G. Wang, Z. Zhu, *Anal. Chem.* 97 (2025) 8755.
[18]M. Nishikawa, T. Kinjyo, T. Ishizaka, S. Beloglazov, T. Takeishi, M. Enoeda, and T. Tanifuji, J. Nucl. Mater. **335,** 70 (2004).
[19]R. G. Wilson, Int. J. Mass Spectrom. Ion Processes **143,** 43 (1995).
[20]W. Jiang, L. Kovarik, M. G. Wirth, Z. Zhu, N. L. Canfield, L. M. Seymour, L. M. Bagaasen, M. E. Bowden, T. Varga, N. R. Overman, Z. Hu, L. Shao, and D. J. Senor, J. Nucl. Mater. **576,** 154281 (2023).
[21]W. Jiang, L. Kovarik, M. G. Wirth, Z. Zhu, J. S. Hardy, Z. Hu, L. Shao, A. M. Casella, and D. J. Senor, J. Nucl. Mater. **613,** 155865 (2025).
[22]D. Pramanik and D. N. Seidman, J. Appl. Phys. **54,** 6352-6367 (1983).
[23]P. Sigmund, *Particle Penetration and Radiation Effects*, Springer, 2006.
[24]W. Eckstein, *Computer Simulation of Ion–Solid Interactions*, Springer Series in Materials Science, 1991.